



Monodisperse SnO_2 anchored reduced graphene oxide nanocomposites as negative electrode with high rate capability and long cyclability for lithium-ion batteries

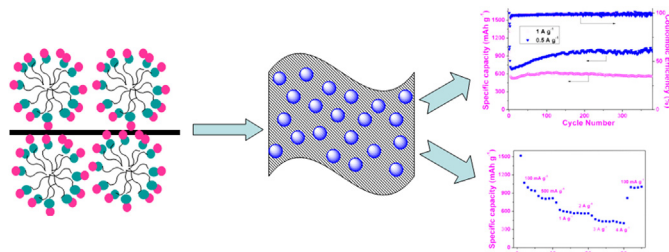
Jinxue Guo, Bin Jiang, Xiao Zhang*, Hongtian Liu

College of Chemistry and Molecular Engineering, Qingdao University of Science and Technology, Qingdao 266042, PR China

HIGHLIGHTS

- Monodisperse SnO_2 anchored rGO composite is synthesized as anode materials.
- Aided with SDS, SnO_2 nanocrystal is dispersed on rGO sheets uniformly and tightly.
- Urea is used to control the precipitation of SnO_2 and reduce GO into rGO.
- The sample shows high capacity, excellent rate capability and cyclic performance.
- TEM images in different charge–discharge cycles reveal the electrode evolution.

GRAPHICAL ABSTRACT



ARTICLE INFO

Article history:

Received 17 January 2014

Received in revised form

28 February 2014

Accepted 19 March 2014

Available online 31 March 2014

Keywords:

Tin oxide

Reduced graphene oxides

Lithium-ion batteries

Anode

Composites

ABSTRACT

In this manuscript, we present a facile and friendly wet chemical method to prepare monodisperse SnO_2 nanocrystals assembled on reduced graphene oxide (RGO). Aided with sodium dodecyl sulfonate, small SnO_2 nanoparticles (~ 5 nm) are deposited onto the flexible support evenly and tightly. A cheap compound, urea, is used for the controlled precipitation of SnO_2 and the reduction of graphene oxide. When tested as the anode material, the hybrid composite electrode delivers excellent cyclability at high current density, such as high reversible capacity over 1000 mAh g^{-1} after 400 cycles at 0.5 A g^{-1} and $\sim 560 \text{ mAh g}^{-1}$ after 400 cycles at 1 A g^{-1} . The composites also exhibit superior rate capability varying from 0.1 to 4 A g^{-1} , and possess capacity of 423 mAh g^{-1} at 4 A g^{-1} . This synthesis strategy seems to be suitable for industrial production and can also be extended to produce a variety of metal oxide/RGO composites.

© 2014 Elsevier B.V. All rights reserved.

1. Introduction

Since their first commercialization about 20 years ago, rechargeable lithium-ion batteries (LIBs) have become the

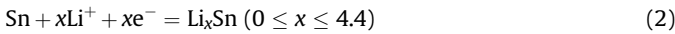
dominant power sources for portable electronic devices, due to their high energy density, fast charge/discharge rate, light weight, and long cycle life. However, the conventional graphite anode, which is limited by its low theoretical capacity of 372 mAh g^{-1} , poor rate capability, and security issue originated from lithium dendrite, cannot fulfill the growing demands for high performance LIBs, especially for the applications in electric vehicles and hybrid electric vehicles [1,2]. Therefore, exploration of the next-generation

* Corresponding author. Tel.: +86 532 84022681; fax: +86 532 84023927.

E-mail address: zhx1213@126.com (X. Zhang).



anode materials with high capacity, excellent rate capability, and high safety has been put on the schedule. For instance, tin oxide (SnO_2) has received special attention, since it is expected to deliver a high theoretical capacity. It is believed that, two principal electrochemical processes including conversion and alloy mechanisms are involved in the SnO_2 -based anode:



Normally, the conversion process of Eq. (1) is thought to be electrochemically irreversible and has no contribution to the reversible capacity, so the theoretical capacity of SnO_2 is calculated to be 790 mAh g^{-1} based on the highly reversible alloy reaction of Eq. (2) [3–6]. Recently, the fully/partially reversible conversion reaction of Eq. (1) has been observed in some nanosized SnO_2 -based anodes [7–10] and the theoretical capacity of SnO_2 can be extended to 1490 mAh g^{-1} accordingly. Unfortunately, the commercialization of SnO_2 anodes for LIBs is still largely hampered by their serious capacity fading upon cycling and/or poor rate capability, mainly ascribing to the large volume changes ($\sim 300\%$) upon Li^+ insertion/extraction [11–14].

To circumvent these issues, various SnO_2 nanostructures have been designed and constructed to improve their electrochemical performance, such as hollow nanostructures [5,15–17], hybrid $\text{Fe}_2\text{O}_3@\text{SnO}_2$ nanorattles [18], nanosheets [4,19], nanoboxes [20], nanotubes [21,22], nanowires [23,24], and nanospheres [25]. SnO_2 has also been incorporated with carbon to prepare SnO_2 -C hybrid electrode materials [26–41], because carbon can not only alleviate the volume change but also result in good electrical contact and enhanced pathways for electronic transport kinetics. Among them, graphene oxide (GO), especially reduced graphene oxide (rGO), has been investigated extensively due to its high surface area, superior electronic conductivity, and excellent mechanical flexibility [5,7,27,32–41]. However, these synthesis processes are commonly time and energy consuming, and associated with complicated and rigorous conditions.

In this work, a facile wet chemical method is employed to synthesize monodisperse SnO_2 /rGO composites (M-SGCs) as schematically illustrated in Fig. 1. Here, urea is used to control the release rate of NH_3 , which promotes the reduction of GO into rGO and precipitates SnO_2 nanoparticles mildly [42]. Sodium dodecyl sulfonate (SDS) plays the key role to anchor SnO_2 nanocrystals on the rGO sheets tightly and insures their even distribution. The resultant M-SGCs that benefit from the highly active monodisperse SnO_2 nanoparticles ($\sim 5 \text{ nm}$), the flexible mechanical support of

rGO sheets, and unhindered electron flow between SnO_2 and rGO, exhibit excellent cyclability at high current density and superior rate capability when tested as anode materials for LIBs.

2. Experimental

2.1. Sample preparation

All reactants are of analytical grade and used as purchased without further purification. GO sheets are first synthesized following a modified Hummers method described elsewhere [43]. In the typical synthesis route of M-SGCs, 0.25 g SDS is dissolved in 7 mL GO dispersion (10 mg mL^{-1}) under magnetic stirring. The mixture is diluted to 30 mL and sonicated for 15 min and then is added into a 10 mL portion of 0.12 M SnCl_4 in 3.8 wt% HCl solution. After 4.8 mL of 1 M urea is added dropwise, the mixture is diluted to 100 mL and is further refluxed at 90°C in a sealed round bottom flask for 16 h. The obtained precipitate is washed with water thoroughly to remove the residual SDS and then dried at 40°C in vacuum. Finally, the sample is sintered at 450°C under an argon atmosphere for 3 h with a heating rate of 2°C min^{-1} to obtain the M-SGCs.

2.2. Materials characterization

The samples are characterized with X-ray powder diffraction (XRD) by a Philips X'pert X-ray diffractometer with $\text{Cu K}\alpha$ radiation ($\lambda = 0.154056 \text{ nm}$). Raman spectroscopy is obtained in the confocal microprobe Raman system (LabRam-010, 632 nm as excitation source). Fourier transform infrared (FTIR) spectra are recorded with FTIR analyzer (Nicolet Magna-IR750). The thermogravimetric (TG) analysis is measured with TG2091F from room temperature to 800°C with a heating rate of $10^\circ\text{C min}^{-1}$ in air. Scanning electron microscope (SEM) is obtained with a JEOL JSM-7500F scanning electron microscope. Transmission electron micrographs (TEM) analysis is performed with FEI TECNAI F30.

The electrochemical tests are carried out with the CR2016-type coin cell. Metallic lithium sheet is used as negative electrodes. The working electrode is fabricated by compressing a mixture of M-SGCs, conductive material (acetylene black) and binder polyvinylidene fluoride (PVDF) in a weight ratio of 8:1:1 onto a copper foil. The electrode is dried at 120°C for 24 h in vacuum oven and the cell assembly is operated in a glove box filled with pure argon. The Clegard 2300 microporous film is used as the separator. The electrolyte solution is 1 M LiPF_6 dissolved in a mixture of ethylene carbonate (EC)/dimethyl carbonate (DMC)/ethyl methyl carbonate (EMC) (1:1:1 in volume) (Zhangjiagang, China). Charge–discharge experiments are performed between 3 and 0.01 V with the LAND CT2001A Battery Cycler (Wuhan China). Cyclic voltammetry (CV) measurements are characterized using a three-electrode cell and metallic lithium is used as the counter and reference electrode. The experiments are performed on CHI660A (CH Instruments, China) over the potential range from 0.01 to 2.0 V vs. Li^+/Li at a scan rate of 0.1 mV s^{-1} .

3. Results and discussion

The overall synthetic solution of M-SGCs is illustrated in Fig. 1. Firstly, a certain concentration of SDS molecules in aqueous solution tends to form micelle with the hydrophilic ends outside [44]. After the addition of Sn^{4+} , SDS[–] absorbs Sn^{4+} cations using its naked anion. Then the micelles with highly positively charged Sn^{4+} anchor tightly onto the surface of GO sheets through the strong electrostatic interaction, which are negatively charged under aqueous solution. On the other hand, the repulsive force between

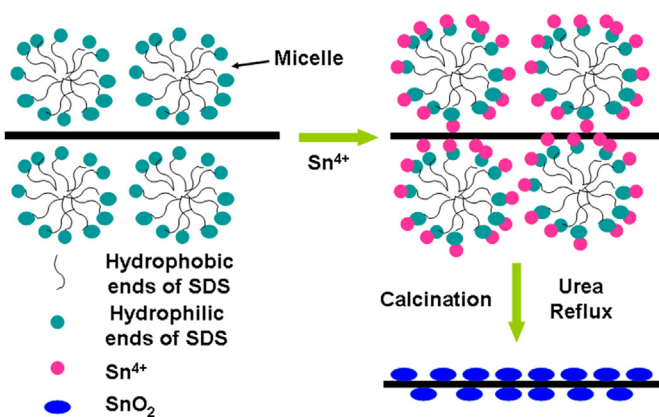


Fig. 1. Schematic diagram for the synthesis route of M-SGCs.

the micelles guarantees their uniformly monodispersion on the sheets surface. Subsequently, the released NH_3 during the reflux step transforms Sn^{4+} into the SnO_2 nanoparticles. Simultaneously, GO is reduced to rGO. After calcination, the final M-SGCs are obtained.

The crystal structure of M-SGCs is characterized with powder XRD and shown in Fig. 2a. All the diffraction peaks in the M-SGCs are assigned to a tetragonal phase SnO_2 with space group $P42mm$. (JCPDS card no. 41–1445). There is no other impurity peaks observed, indicating the high phase purity of the product. The good crystallization is proved by the intense and sharp reflection peaks. Calculated from the broaden peak of (110) with Debye–Scherrer equation, the mean particle size of SnO_2 in M-SGCs is evaluated to be about 5.2 nm. Interestingly, the peak of rGO in the composite is not observed. As shown in Fig. 2a, the rGO sheets show the typical peak centered at 2θ of 24.6°, indicating its successful reduction. However, the diffraction density of pure rGO is much lower compared with that of SnO_2 , and the peak position of rGO (24.6°) is close to the (110) peak of SnO_2 (26.5°) (see supporting information Fig. S1). So the peak of rGO and (110) peak of SnO_2 are overlapped in the XRD pattern of the composite (see supporting information Fig. S2), thus inducing the absence of rGO peak.

The structure of M-SGCs is also investigated with Raman spectroscopy. As is shown in Fig. 2b, the Raman spectrum of GO shows two characteristic peaks located at about 1330 cm^{-1} (D band, corresponding to κ -point phonons of A_{1g} symmetry) and 1590 cm^{-1} (G band, corresponding to an E_{2g} phonon of sp^2 -bonded carbon atoms). In the Raman spectrum of M-SGCs, the characteristic peaks of D band and G band for GO are observed at about 1325 and 1590 cm^{-1} , respectively. The peaks located at about 620 and 775 cm^{-1} , corresponding to the expansion and contraction vibration modes of Sn–O bonds in tetragonal SnO_2 , should be assigned to the A_{1g} and B_{2g} symmetry of SnO_2 [45]. This result confirms the presence of SnO_2 in the composites. It is generally accepted that the

intensity ratio of the D to G band ($I_{\text{D}}:I_{\text{G}}$) can reflect the disorder and defects of carbonaceous materials [46–48]. The $I_{\text{D}}:I_{\text{G}}$ of M-SGCs is calculated to be 1.09, which is higher than that of GO (0.95). It should be ascribed to the reduction of GO into rGO by urea [42,48].

The formation of M-SGCs and the reduction of the GO in the composites are further confirmed with FTIR techniques. As is shown in Fig. 2c, the characteristic FTIR bands of GO are centered at 1720, 1625, 1579, 1399, 1223, and 1050 cm^{-1} , corresponding to the stretching vibration of $\text{C}=\text{O}$ (carboxyl), $\text{C}=\text{O}$ (epoxy), skeletal ring vibrations, $\text{O}=\text{H}$ (carboxyl), $\text{C}=\text{OH}$ (hydroxyl), and $\text{C}=\text{O}$ (carboxyl or alkoxy), respectively [34,37]. In the FTIR spectrum of M-SGCs, no characteristic peaks of SDS are observed. In comparison with the spectrum of GO, the peaks related to $\text{C}=\text{O}$, $\text{C}=\text{O}$, and $\text{O}=\text{H}$ bands are absent, suggesting the removal of most oxygen functionalities and the reduction of GO. The presence of the intense bands located at 1567 cm^{-1} , where the $\text{C}=\text{C}$ stretching vibration of benzene usually appears, indicates the healing of the basal structure of the graphite domains. The intense bands at around 630 cm^{-1} observed in the M-SGCs should be assigned to the asymmetric and symmetric vibrations of $\text{Sn}=\text{O}=\text{Sn}$, confirming the formation of the M-SGCs. As is shown in TG curve (Fig. 2d), the weight loss of 34% implies that the weight portion of SnO_2 is higher than 60% in the composite.

The morphology of the resultant M-SGCs is examined with SEM and TEM measurements and is shown in Fig. 3. As shown in the SEM image (Fig. 3a), M-SGCs show crumpled layer structures, consisting of various rGO sheets arranged in a disordered manner. The bright area reveals the dense regions of SnO_2 nanocrystals [49,50]. The TEM images (Fig. 3b, c) reveal that monodisperse nanocrystals are homogeneously distributed on the rGO sheets. The average particle size of SnO_2 nanocrystals extracted from these images is about $\sim 5\text{ nm}$, which is in good agreement with the XRD results. In contrast with it, the TEM image (Fig. 3d) of SnO_2 –rGO hybrid composites (SGCs), which is synthesized without SDS, shows uneven dispersion of SnO_2 particles on rGO layer. In one

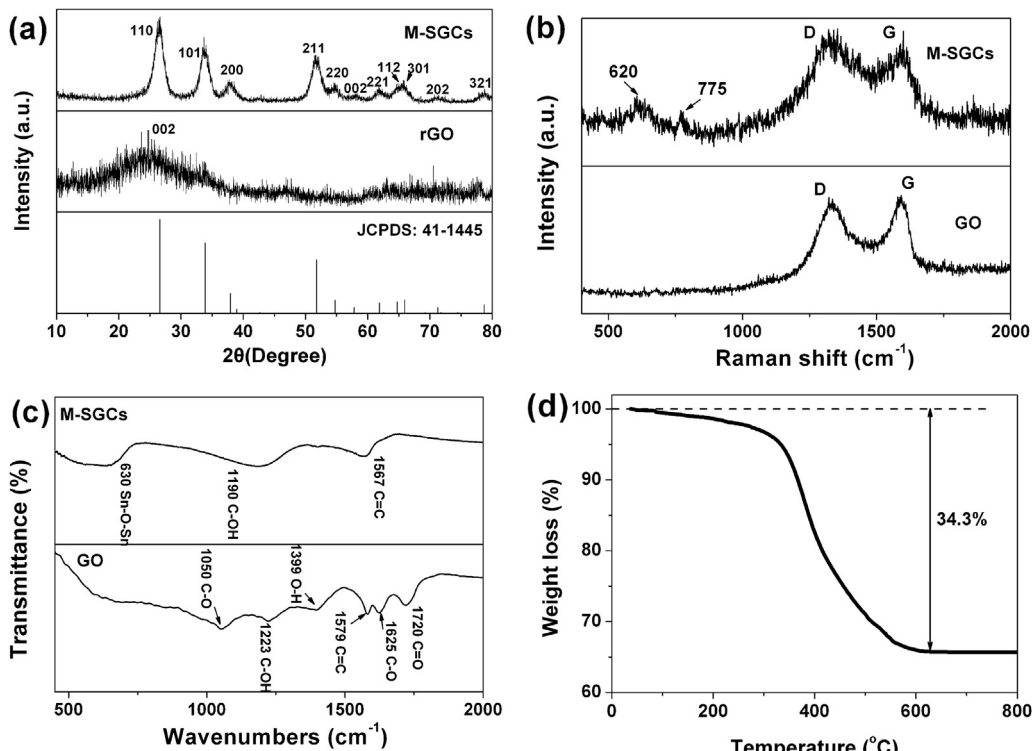


Fig. 2. (a) XRD patterns of as-prepared M-SGCs and rGO. (b) Raman spectra and (c) FTIR spectra of M-SGCs and GO. (d) TG curve of M-SGCs.

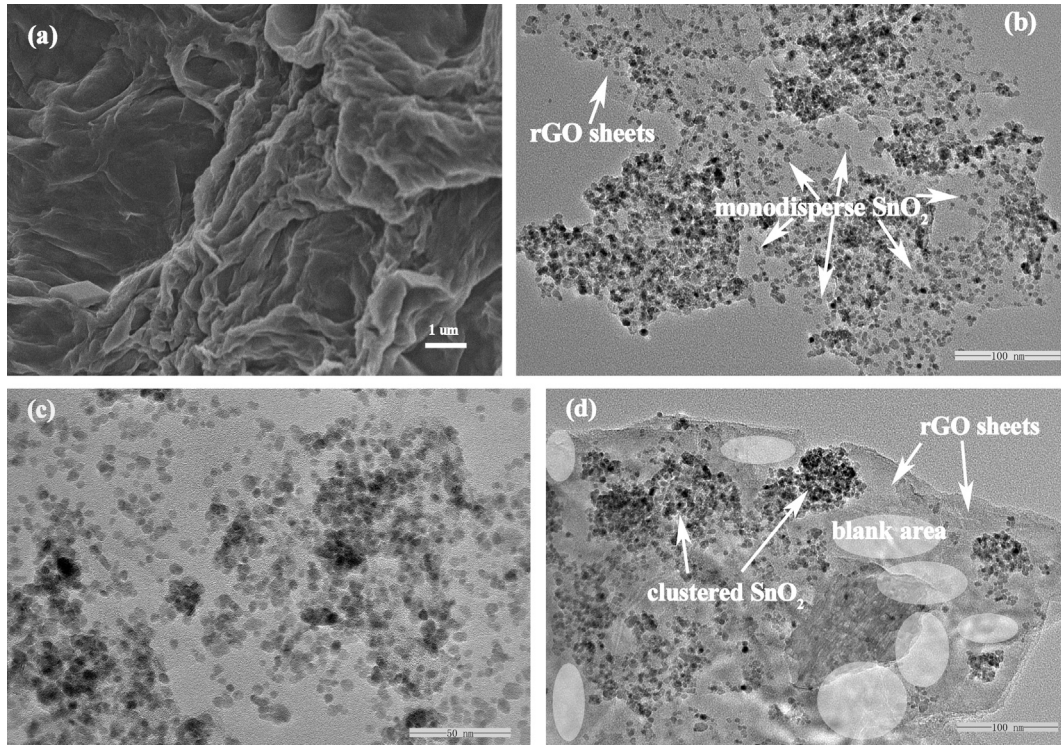


Fig. 3. (a) SEM and (b, c) TEM images of M-SGCs. (d) TEM image of SGCs.

hand, part of rGO sheet surface is blank without the distribution of SnO_2 . On the other hand, clustered nanocrystals are observed in certain areas. This result suggests that the addition of SDS is beneficial for the monodispersing distribution of SnO_2 nanocrystals.

The Li^+ storage properties of the obtained M-SGCs are investigated as anode materials for LIBs with the laboratory Li^+ half-cell configuration. Fig. 4a presents the CV curves of M-SGCs at a scan rate of 0.1 mV s^{-1} between 0.01 and 2 V vs. Li^+/Li . In the first cycle, two sharp cathodic peaks at 0.85 and 0.12 V can be ascribed to the formation of Li_2O and the lithium alloying reaction with Sn, respectively [36,51]. And the small cathodic peak at 0.46 V is related to the decomposition of the electrolyte on the surface of the SnO_2 nanoparticles and rGO in the formation process of solid electrolyte interface (SEI) layer [7,32,52]. In addition, the anodic peaks at around 0.58 V and 1.3 V can be assigned to the de-alloying of Li_xSn and Li_2O to SnO_2 , respectively [7–9]. The latter oxidation peak (1.3 V) strongly indicates that the conversion reaction of Eq. (1) takes place reversibly during the charge/discharge process of M-SGCs anode. The corresponding slopes and plateau also exist in the 1st and 2nd galvanostatic charge–discharge profiles of M-SGCs electrode (Fig. 4b). It can be clearly observed that, M-SGCs show a first discharge capacity of 1515 mAh g^{-1} and a charge capacity of 1010 mAh g^{-1} at a current density of 100 mA g^{-1} . The relatively low coulombic efficiency (about 67%) in the first cycle is ascribed to the irreversible formation of amorphous lithium oxide and the decomposition of electrolyte and lithium salt in the formation of SEI layer.

The cyclic performances of the M-SGCs and SGCS electrodes at a relatively high current density of 0.5 A g^{-1} are shown in Fig. 4c. The discharge capacities of SGCS fade dramatically from 754 (the second cycle) to 233 mAh g^{-1} in the 200th cycle, delivering poor capacity retention of 31%. In comparison, the discharge capacities of M-SGCs electrode decrease slightly from 1057 (the second cycle) to 961 mAh g^{-1} in the 200th cycle, showing higher capacity retention of 91%. Furthermore, it exhibits a comparatively high capacity of

1036 mAh g^{-1} with the capacity retention of 98% in the 400th cycle (shown below in Fig. 4d). It can be clearly observed that the M-SGCs electrode exhibits improved cyclic stability than that of SGCS electrode, which should be attributed to the monodispersing of SnO_2 nanoparticles in the M-SGCs achieved with the aid of SDS.

With the aim to further explore the high rate capability of M-SGCs anode, the cyclic performance at high current densities of 0.5 and 1 A g^{-1} are tested, respectively. As is shown in Fig. 4d, M-SGCs anode delivers an excellent cyclic performance at 0.5 A g^{-1} . After initial several conditioning cycles, its discharge capacity shows obvious increase. The stable capacity over 790 mAh g^{-1} (theoretical capacity based on an alloy mechanism) is obtained after 53 cycles and reaches 1036 mAh g^{-1} in the 400th cycle. This interesting capacity increase should be assigned to the contribution of the improved conversion reaction ($\text{SnO}_2 + 4\text{Li}^+ + 4\text{e}^- = \text{Sn} + 2\text{Li}_2\text{O}$). With the increasing electrochemical cycles, the pulverization of electrode materials will make the in-situ formed Sn nanoparticles smaller and smaller. It is believed that, the decrease of reagent particle size could reduce the activation energy for solid-state double decomposition reactions, thus boosting the conversion reaction and contributing to the reversible capacity. And the excellent cyclic performance is also observed at higher current density of 1 A g^{-1} . M-SGCs deliver superior cyclic capability over 560 mAh g^{-1} for a long life beyond 400 cycles. In the meanwhile, the M-SGCs anode shows excellent coulombic efficiency at both the current densities. The M-SGCs show initial coulombic efficiencies of 63 and 54% at 0.5 and 1 A g^{-1} , respectively. After several cycles, both the coulombic efficiencies reach up and maintain higher than 98% throughout the 400 cycles. Thus, it can be concluded that the M-SGCs electrode delivers a superior cycling performance as well as high coulombic efficiency at high rate charge/discharge process.

It is worth noting that the specific capacity values are estimated based on the total mass of the M-SGCs. In order to evaluate the contribution of SnO_2 in the M-SGCs, the discharge capacities at 0.5 A g^{-1} are calculated based on the mass of SnO_2 (66%). The weight

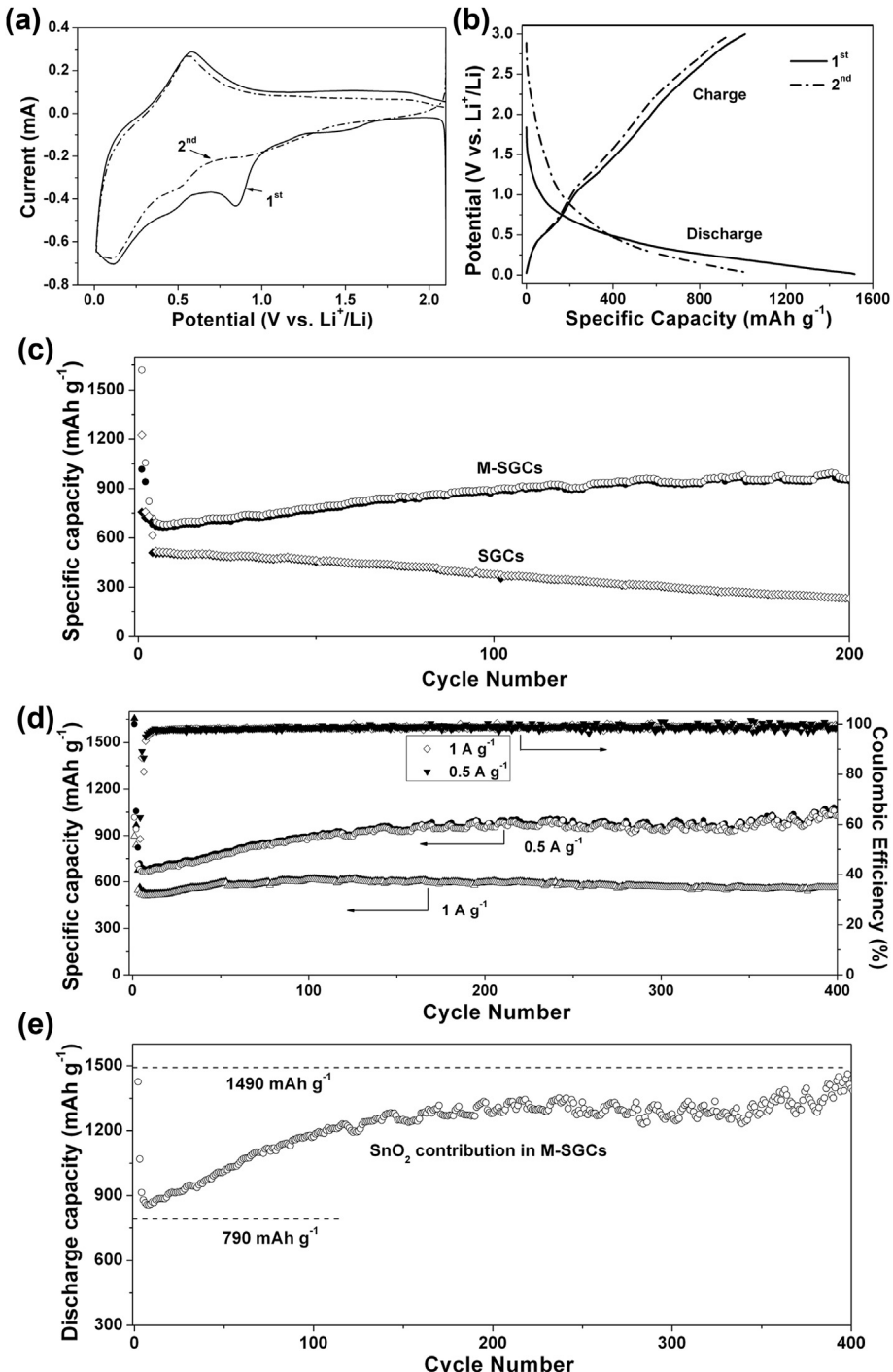


Fig. 4. (a) Cyclic voltammogram of the M-SGCs electrode at the scanning rate of 0.1 mV s^{-1} . (b) The discharge–charge profiles of M-SGCs at the current density of 100 mA g^{-1} . (c) Cyclic performance of M-SGCs and SGCs at 0.5 A g^{-1} . (d) Cyclic performance of M-SGCs at 0.5 A g^{-1} and 1 A g^{-1} after 2 cycles at 100 mA g^{-1} . (e) Discharge capacities versus cycle numbers of SnO_2 in the M-SGCs.

content of rGO in M-SGCs is 34% based on the TG measurements (Fig. 2d). The capacity of SnO_2 in the hybrid material is calculated as follows: $C_{\text{SnO}_2} = (C_{\text{M-SGCs}} - C_{\text{rGO}} \times 34\%) / 66\%$. The rGO delivers a specific capacity of $\sim 340 \text{ mAh g}^{-1}$ (see supporting information Fig. S3). As is shown in Fig. 4e, the second discharge capacity of SnO_2 is 1425 mAh g^{-1} , which is much higher than the theoretical capacity of 790 mAh g^{-1} (based on the alloy reaction process) and is very close to the theoretical value of 1490 mAh g^{-1} (based on both the conversion and the alloy processes). Moreover, the capacity of SnO_2

in the composites is always higher than 790 mAh g^{-1} , as it can be clearly observed in Fig. 4e. After 400 cycles, the SnO_2 in the M-SGCs delivers a high capacity of 1394 mAh g^{-1} , indicating superior capacity retention of 98%. Thus, the completely reversible electrochemical conversion between SnO_2 and $\text{Li}_{4.4}\text{Sn}$ has been successfully demonstrated in our presented M-SGCs anode. To our best knowledge, the M-SGCs presented here is among the best to prove the highly reversible reaction of SnO_2 -based anode with a long cyclic life up to hundreds of cycles [7,8].

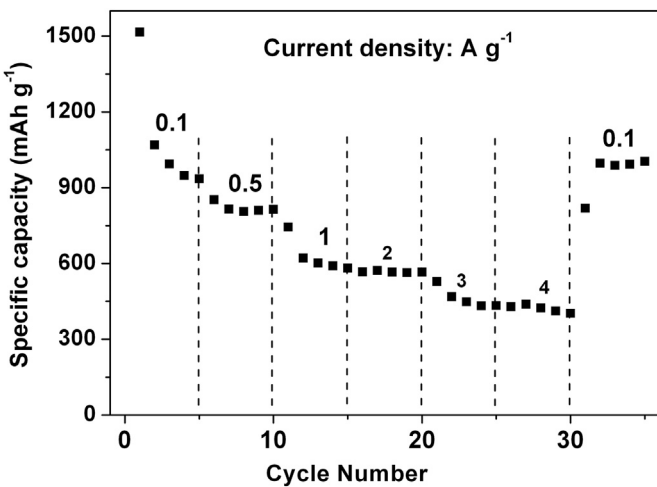


Fig. 5. Rate capability of M-SGCs electrode.

The excellent rate performance of M-SGCs is also observed due to the hybrid benefits of proper chemical components and nano-structures. As shown in Fig. 5, the M-SGCs electrode exhibits superior rate performance when the current densities vary from 0.1, 0.5,

1, 2, 3–4 A g⁻¹. The capacity values can retain as high as 572 and 423 mAh g⁻¹ at rates of 2 and 4 A g⁻¹, respectively. Remarkably, after this rigorous test process, the M-SGCs anode can recover to its initial value of 1004 mAh g⁻¹ when the current density returns to 0.1 A g⁻¹, exhibiting good capacity retention ability.

The superior electrochemical performance of the M-SGCs anode is compared with the data that have been reported recently in Table 1. These data about the Li⁺ storage properties of SnO₂-based materials mainly focus on their long life cycles (≥ 50 cycles) performance as the anode. It is shown that SnO₂/graphene composites presented by Lin et al. exhibit high capacity at high rate of 2 A g⁻¹ [40], which is similar to the value of the M-SGCs. But its reversible capacity and cycling life obtained at lower discharge rate is inferior to those of M-SGCs. The M-SGCs also exhibit better electrochemical performance than the data that have been marked in Ref. [8,9,33,38,39], which are the exciting results for SnO₂-based anode that have been presented recently. Zhou et al. have reported the highest capacity that has been reported for SnO₂ anode materials [7]. The presented M-SGCs exhibit comparable capacity and cyclic stability to the data at rate of 0.5 A g⁻¹ in [7]. Although they obtain slightly higher reversible capacity at higher rate of 1 A g⁻¹, the corresponding cyclic performance is absent. However, the M-SGCs anode delivers outstanding cycling stability (567 mAh g⁻¹ at 400 cycles) at 1 A g⁻¹. Thus, the electrochemical performance of the

Table 1

Comparison of the electrochemical performance of the M-SGCs electrode with those of SnO₂ based electrodes reported in the literature.

Samples	Synthesis method	Current rate (mA g ⁻¹)	Discharge capacity (mAh g ⁻¹)	Capacity retention (mAh g ⁻¹)/(cycles)	Ref./publication year
M-SGCs	Reflux	500 1000 2000 3000 4000	1057 (2nd) 968 (2nd) 571 528 439	1036/400 567/400	Present work
SnO ₂ /Cu		200	713	535/150	[41]/2013
SnO ₂ /graphene		100 2000	1130 580	825/50	[40]/2013
SnO ₂ /graphene	Hydrothermal	100 1000 2000		800/200 600/50 400/100	[39]/2013
SnO ₂ /graphene		100 500	931	718/200 514/200	[38]/2013
SnO ₂ /graphene	Hydrothermal	~78		847/50	[37]/2013
SnO ₂ /graphene	Hydrothermal	100 200	907 659	710/50 575/50	[36]/2012
SnO ₂ /graphene	Hydrothermal	3200		380/50	[35]/2012
SnO ₂ /graphene	Precipitation	100	950	775/50	[34]/2011
SnO ₂ /graphene	Reflux	100 50		872/200 910/50	[33]/2013 [32]/2012
SnO ₂ /carbon nanofiber		100		383/30	[31]/2012
SnO ₂ /CNT		25		650/100	[30]/2012
SnO ₂ /CNT	Solvothermal	200		497/300	[29]/2011
SnO ₂ /graphene	Hydrothermal	400		518/50	[28]/2011
SnO ₂ /graphene		50	1080	649/30	[27]/2011
SnO ₂ /graphene	Hydrothermal	~156	786	558/50	[26]/2010
SnO ₂ nanorod array	Solvothermal	7820	720	590/20	[24]/2013
CNT@SnO ₂ nanotube		~390	586	542/200	[22]/2006
SnO ₂ nanoboxes		~156		570/40	[20]/2011
SnO ₂ nanosheets	Hydrothermal	156	762	534/50	[19]/2012
Fe ₂ O ₃ @SnO ₂ nanorattles		200	865	419/30	[18]/2009
Double-shelled SnO ₂	Spray	625 3125	704 418	642/40 392/40	[17]/2013
SnO ₂ @C		200 1000	978 (2nd) 770	1039/100	[9]/2012
SWNTs@ SnO ₂ @PPy		150 1000 3000	1314 (1st) 553/100	823/100	[8]/2012
SnO ₂ /graphene	Lyophilization	500 1000 10A	1865 (1st) 994 631	1021/500	[7]/2013
SnO ₂ /graphene	Hydrothermal	500		696/300	[5]/2012
SnO ₂ nanosheets		78.2		559/20	[4]/2010

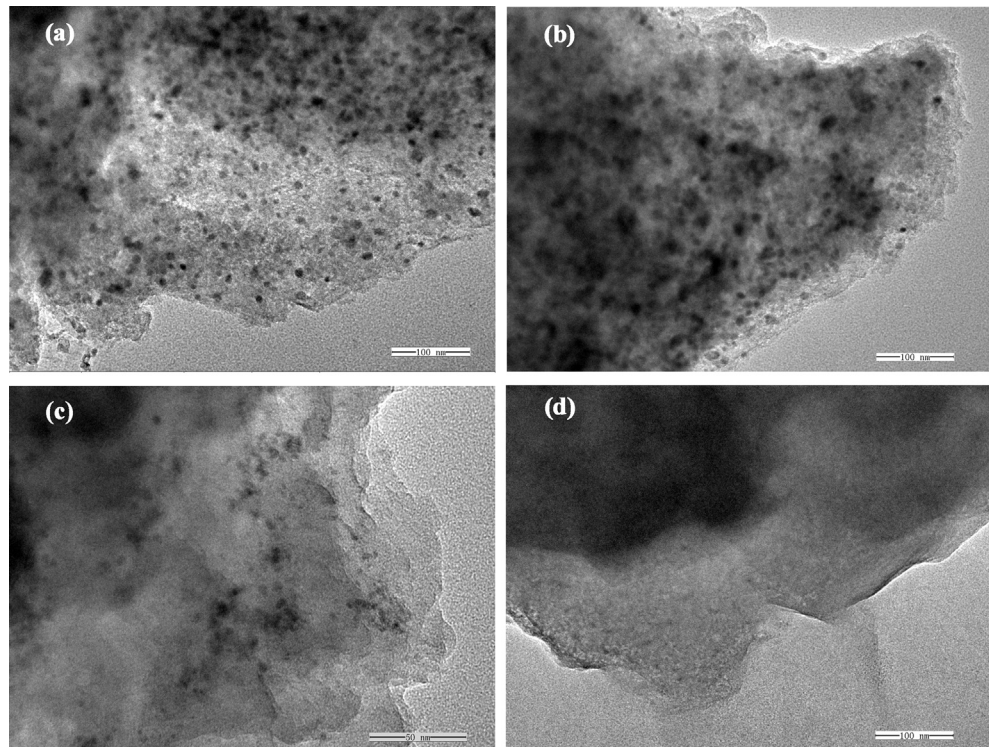


Fig. 6. TEM images of M-SGCs after 151 (a), 304 (b), and 475 (c) charge–discharge cycles at 0.5 A g^{-1} . (d) TEM image of SGCS after 147 charge–discharge cycles at 0.5 A g^{-1} .

M-SGCs, especially the high rate capability and long cyclic stability, is better than most of the SnO_2 -based anodes ever reported, and can be a promising candidate for the next-generation of anode materials for high performance LIBs.

In order to explore the root of the excellent cycling stability of the M-SGCs, TEM images of M-SGCs after 151, 304, and 475 cycles of charge–discharge test at 0.5 A g^{-1} are obtained and compared in Fig. 6a–c. The TEM image (Fig. 6d) of SGCS after 147 charge–discharge cycles at 0.5 A g^{-1} is also presented for comparison. As shown in Fig. 6a, SnO_2 nanocrystals are uniformly distributed on the rGO sheets, indicating that M-SGCs can maintain its structure after 151 cycles. After 304 charge–discharge cycles, the boundaries of SnO_2 nanoparticles become blurry (Fig. 6b), suggesting that these particles tend to fuse together with repeated volume changes. But it is notable that, the surface of rGO sheets are enveloped with SnO_2 , and the capacity of M-SGCs in the 304th cycle shows no fade. All these phenomena reveal that no SnO_2 particles break away from rGO sheets, confirming the tight interaction between them. After 475 cycles, less SnO_2 nanoparticles are observed on the surface of rGO sheets (Fig. 6c), indicating the electrode collapse. For SGCS, almost no SnO_2 nanoparticles can be observed on rGO sheets only after 147 cycles (Fig. 6d), which suggests that the interaction between SnO_2 nanoparticles and rGO sheets is very weak without the addition SDS during the synthesis process. This result reveals that SDS plays the key role to anchor SnO_2 nanoparticles tightly on the surface of rGO sheets to improve the cycling life of the electrode materials.

The superior Li^+ storage performance of M-SGCs including high reversible capacity, high rate capability and long cycling life may be attributed to the following benefits. (1) The monodispersion of SnO_2 nanoparticles ensures the isolation of SnO_2 nanoparticles and is beneficial for the suppression of their aggregation during electrochemical charge/discharge process, resulting in improved cycling stability. (2) The tight contact between SnO_2 nanoparticles and rGO sheets can effectively anchor SnO_2 nanocrystals on the

surface of rGO sheets, and thus prevents the aggregation of Sn nanoparticles and suppresses the mechanical loss of active materials in contact with the rGO sheets. (3) The guaranteed extremely small size of active materials can supply large specific surface area and abundant active sites for full utilization of active materials, and achieve high reversible conversion storage of Li^+ . (4) Moreover, the initiate connection between SnO_2 and rGO makes electron flowing from rGO sheets, which is famous for its good electronic conductivity and high surface areas, to the surface of SnO_2 fast and smooth, leading to enhanced reversible capacity.

4. Conclusions

In summary, with the aid of the binding molecule of SDS and the reducing agent of urea, small SnO_2 nanoparticles have been controllably anchored on the flexible rGO support evenly and tightly for the formation of monodisperse SnO_2 /rGO hybrid composites. Benefiting from the monodispersion of the nanosized SnO_2 particles ($\sim 5 \text{ nm}$), the highly conductivity and flexible mechanical property of rGO sheets, and the close interaction between SnO_2 nanocrystals and rGO, the resultant M-SGCs deliver superior electrochemical performance in terms of cyclic stability and cycling life as well as rate capability for LIBs. Most importantly, this synthesis strategy, the desirable anchor of monodisperse SnO_2 nanocrystals onto rGO sheets through a facile and friendly wet chemical route, is a versatile approach to promote the electrochemical performance of other metal oxides and can be scaled up easily for industrial production.

Acknowledgments

This work was financially supported by National Natural Science Foundation of China (21003079), Natural Science Foundation (ZR2011BM018), Research Award Fund for Outstanding Middle-Aged and Young Scientist (BS2011CL020) of Shandong

Province and Qingdao Project of Science and Technology (12-1-4-3-(20)-jch).

Appendix A. Supplementary data

Supplementary data related to this article can be found at <http://dx.doi.org/10.1016/j.jpowsour.2014.03.085>.

References

- [1] J.M. Tarascon, M. Armand, *Nature* 414 (2001) 359–367.
- [2] P.G. Bruce, B. Scrosati, J.M. Tarascon, *Angew. Chem. Int. Ed.* 47 (2008) 2930–2946.
- [3] X.W. Lou, C.M. Li, L.A. Archer, *Adv. Mater.* 21 (2009) 2536–2539.
- [4] C. Wang, Y. Zhou, M. Ge, X. Xu, Z. Zhang, J.Z. Jiang, *J. Am. Chem. Soc.* 132 (2010) 46–47.
- [5] X. Zhou, Y.X. Yin, L.J. Wan, Y.G. Guo, *J. Mater. Chem.* 22 (2012) 17456–17459.
- [6] L. Ji, Z. Lin, M. Alcoutabi, X. Zhang, *Energy Environ. Sci.* 4 (2011) 2682–2699.
- [7] X. Zhou, L.J. Wan, Y.G. Guo, *Adv. Mater.* 25 (2013) 2152–2157.
- [8] Y. Zhao, J. Li, N. Wang, C. Wu, G. Dong, L. Guan, *J. Phys. Chem. C* 116 (2012) 18612–18617.
- [9] F. Han, W.C. Li, M.R. Li, A.H. Lu, *J. Mater. Chem.* 22 (2012) 9645–9651.
- [10] J. Guo, L. Chen, G. Wang, X. Zhang, F. Li, *J. Power Sources* 246 (2014) 862–867.
- [11] D. Deng, J.Y. Lee, *Chem. Mater.* 20 (2008) 1841–1846.
- [12] L. Cui, J. Shen, F. Cheng, Z. Tao, J. Chen, *J. Power Sources* 196 (2011) 2195–2201.
- [13] J.Y. Huang, L. Zhong, C.M. Wang, J.P. Sullivan, W. Xu, L.Q. Zhang, S.X. Mao, N.S. Hudak, X.H. Liu, A. Subramanian, H. Fan, L. Qi, A. Kushima, J. Li, *Science* 330 (2010) 1515–1520.
- [14] C.M. Wang, W. Xu, J. Liu, J.G. Zhang, L.V. Saraf, B.W. Arey, D. Choi, Z.G. Yang, J. Xiao, S. Thevuthasan, D.R. Baer, *Nano Lett.* 11 (2011) 1874–1880.
- [15] X.W. Lou, Y. Wang, C. Yuan, J.Y. Lee, L.A. Archer, *Adv. Mater.* 18 (2006) 2325–2329.
- [16] X.W. Lou, C. Yuan, L.A. Arvher, *Adv. Mater.* 19 (2007) 3328–3332.
- [17] Y.J. Hong, M.Y. Son, Y.C. Kang, *Adv. Mater.* 25 (2013) 2279–2283.
- [18] J.S. Chen, C.M. Li, W.W. Zhou, Q.Y. Yan, L.A. Archer, X.W. Lou, *Nanoscale* 1 (2009) 280–285.
- [19] C. Wang, G. Du, K. Ståhl, H. Huang, Y. Zhong, J.Z. Jiang, *J. Phys. Chem. C* 116 (2012) 4000–4011.
- [20] Z. Wang, D. Luan, F.Y.C. Boey, X.W. Lou, *J. Am. Chem. Soc.* 133 (2011) 4738–4741.
- [21] Y. Wang, J.Y. Lee, H.C. Zeng, *Chem. Mater.* 17 (2005) 3899–3903.
- [22] Y. Wang, H.C. Zeng, J.Y. Lee, *Adv. Mater.* 18 (2006) 645–649.
- [23] M.S. Park, G.X. Wang, Y.M. Kang, D. Wexler, S.X. Dou, H.K. Liu, *Angew. Chem. Int. Ed.* 119 (2007) 764–767.
- [24] S. Chen, M. Wang, J. Ye, J. Cai, Y. Ma, H. Zhou, L. Qi, *Nano Res.* 6 (2013) 243–252.
- [25] R. Demir-Cakan, Y.S. Hu, M. Antonietti, J. Maier, M.M. Titirici, *Chem. Mater.* 20 (2008) 1227–1229.
- [26] L.S. Zhang, L.Y. Jiang, H.J. Yan, W.D. Wang, W. Wang, W.G. Song, Y.G. Guo, L.J. Wan, *J. Mater. Chem.* 20 (2010) 5462–5467.
- [27] X. Zhu, Y. Zhu, S. Murali, M.D. Stoller, R.S. Ruoff, *J. Power Sources* 196 (2011) 6473–6477.
- [28] S. Ding, D. Luan, F.Y.C. Boey, J.S. Chen, X.W. Lou, *Chem. Commun.* 47 (2011) 7155–7157.
- [29] J. Ren, J. Yang, A. Abouimrane, D. Wang, K. Amine, *J. Power Sources* 196 (2011) 8701–8705.
- [30] D. Ahn, X. Xiao, Y. Li, A.K. Sachdev, H.W. Park, A. Yu, Z. Chen, *J. Power Sources* 212 (2012) 66–72.
- [31] W. Xia, Y. Wang, Y. Luo, J. Li, Y. Fang, L. Gu, J. Peng, J. Sha, *J. Power Sources* 217 (2012) 351–357.
- [32] X. Wang, X. Cao, L. Bourgeois, H. Guan, S. Chen, Y. Zhong, D.M. Tang, H. Li, T. Zhai, L. Li, Y. Bando, D. Golberg, *Adv. Funct. Mater.* 22 (2012) 2682–2690.
- [33] S.J.R. Prabakar, Y.H. Hwang, E.G. Bae, S. Shim, D. Kim, M.S. Lah, K.S. Sohn, M. Pyo, *Adv. Mater.* 25 (2013) 3307–3312.
- [34] B. Zhao, G. Zhang, J. Song, Y. Jiang, H. Zhuang, P. Liu, T. Fang, *Electrochim. Acta* 56 (2011) 7340–7346.
- [35] C. Xu, J. Sun, L. Gao, *J. Mater. Chem.* 22 (2012) 975–979.
- [36] S.K. Park, S.H. Yu, N. Pinna, S. Woo, B. Jang, Y.H. Chung, Y.H. Cho, Y.E. Sung, Y. Piao, *J. Mater. Chem.* 22 (2012) 2520–2525.
- [37] S. Yang, W. Yue, J. Zhu, Y. Ren, X. Yang, *Adv. Funct. Mater.* 23 (2013) 3570–3576.
- [38] L. Wang, D. Wang, Z. Dong, F. Zhang, J. Jin, *Nano Lett.* 13 (2013) 1711–1716.
- [39] Y. Fang, B. Luo, Y. Jia, X. Li, B. Wang, Q. Song, F. Kang, L. Zhi, *Adv. Mater.* 24 (2012) 6348–6355.
- [40] J. Lin, Z. Peng, C. Xiang, G. Ruan, Z. Yan, D. Natelson, J.M. Tour, *ACS Nano* 7 (2013) 6001–6006.
- [41] J. Deng, C. Yan, L. Yang, S. Baunack, S. Oswald, H. Wendrock, Y. Mei, O.G. Schmidt, *ACS Nano* 7 (2013) 6948–6954.
- [42] Z. Lei, L. Lu, X.S. Zhao, *Energy Environ. Sci.* 5 (2012) 6391–6399.
- [43] J. Guo, B. Jiang, X. Zhang, X. Zhou, W. Hou, *J. Solid State Chem.* 205 (2013) 171–176.
- [44] W. Zhou, J. Liu, T. Chen, K.S. Tan, X. Jia, Z. Luo, C. Cong, H. Yang, C.M. Li, T. Yu, *Phys. Chem. Chem. Phys.* 13 (2011) 14462–14465.
- [45] L.L. Li, W.M. Zhang, Q. Yuan, Z.X. Li, C.J. Fang, L.D. Sun, L.J. Wan, C.H. Yan, *Cryst. Growth Des.* 8 (2008) 4165–4172.
- [46] M. Zhang, B. Qu, D. Lei, Y. Chen, X. Yu, L. Chen, Q. Li, Y. Wang, T. Wang, *J. Mater. Chem.* 22 (2012) 3868–3874.
- [47] R.I. Jafri, N. Rajalakshmi, S. Ramaprabhu, *J. Mater. Chem.* 20 (2010) 7114–7117.
- [48] Z. Lin, G. Waller, Y. Liu, M. Liu, C.P. Wong, *Adv. Energy Mater.* 2 (2012) 884–888.
- [49] H. Song, N. Li, H. Cui, C. Wang, *J. Mater. Chem. a* 1 (2013) 7558–7562.
- [50] X. Zhao, C.M. Hayner, M.C. Kung, H.H. Kung, *Chem. Commun.* 48 (2012) 9909–9911.
- [51] J.C. Lytle, H. Yan, N.S. Ergang, W.H. Smyrl, A. Stein, *J. Mater. Chem.* 14 (2004) 1616–1622.
- [52] H. Wang, L.F. Cui, Y. Yang, H.S. Casalongue, J.T. Robinson, Y. Liang, Y. Cui, H. Dai, *J. Am. Chem. Soc.* 132 (2010) 13978–13980.